Ultramicroscopy 20 (1986) 279–292
North-Holland, Amsterdam

COMPUTER SIMULATION OF DIFFRACTION CONTRAST IMAGES AND LATTICE FRINGE PATTERNS OF SMALL HEXAGONAL DISLOCATION LOOPS

R. HILLEBRAND, K. SCHEERSCHMIDT and J. HEYDENREICH

Institut für Festkörperphysik und Elektronenmikroskopie der Akademie der Wissenschaften der DDR, Weinberg 2, Halle DDR-4020, German Dem. Rep.

Received 22 May 1986

Dedicated to Professor Ernst Ruska on the occasion of his 80th birthday

Diffraction contrast and lattice fringe images of small hexagonal dislocation loops are investigated by computer simulation combining the diffraction contrast calculation with the Fourier formalism for considering the electron-optical imaging process including aberrations. Simulated images are presented applying this method to investigate systematically the nature of a small prismatic dislocation loop of Frank type inclined to the electron beam. In particular, the relations between the black-white diffraction contrast oscillations and the lattice fringe distortions (including shifting, bending and termination) have been studied in connection with the variations in the contrast of loops with the thickness of the foil, the depth of the defect in the foil, the deviation from the Bragg reflection condition and the influence of image aberrations.

1. Introduction

In a previous paper [1] a method was described combining the calculation of diffraction contrast amplitudes with the Fourier transformation formalism for simulating bright- or dark-field diffraction contrasts and lattice fringe images of arbitrarily small crystal defects. In the present work the method of ref. [1] is applied to simulate bright- and dark-field images as well as lattice fringe patterns of a small, inclined, hexagonally shaped, prismatic dislocation loop to derive general rules of the behaviour of lattice fringe contrast with respect to the defect nature and the imaging parameters. As in ref. [2], the outward or inward bendings of fringes caused by the dislocation loop no longer prove unequivocally the defect to be of interstitial or of vacancy type. Nevertheless, comprehensive systematic analysis of the fringe distortions (shifting, bending and termination) with respect to the behaviour of the black-white contrast oscillation in bright- and dark-field diffraction contrast should yield information on the local defect structure.

For sufficiently small dislocation loops, comparable to small defect clusters and precipitates, the black–white (BW) contrast method has been shown to be useful for defect identification (analysis of BW oscillations, cf., e.g., refs. [3–5] and the review [6]). This oscillation behaviour can be studied in a very illustrative manner using computer-simulated catalogues calculated on the basis of the infinitesimal loop approximation [7], which enables the results to be extended to finite diameters when different additional effects are studied separately. The shape of the BW contrast is mainly determined by the long-range part of the elastic distortion field, i.e., it depends solely on the effective strain field of the loop and the elastic moduli of the anisotropic matrix [8].

The BW contrast method fails for very small defects or if the specimen is so thin that anomalous absorption is negligible. Appropriate extreme defocusing (some μm) of the objective lens, however, allows one to transfer the phase information into interpretable black–white contrasts [9]. In this way the BW analysis is extended to cases of vanishing diffraction contrast taking into account the modified oscillation behaviour.

For loops of non-circular geometry the funda-

0304-3991/86/$03.50

mental contrast properties are, in principle, the same as for the infinitesimal loop approximation. The line of no contrast and the BW vector are less influenced by the loop shape. However, the line of no contrast, for instance, is only straight and perpendicular to the reflection $\boldsymbol{g}$ if the reflecting plane is a symmetry plane of the defect. Furthermore, non-circular shapes mainly influence the central region of the loop image; here the associated characteristic contrast features are called fine details. The fine details result from overlapping contrasts of different parts of the central loop region. These patterns are strongly influenced by even weak image aberrations (defocus of some 10 nm) where the long-range BW behaviour does not change. To avoid misinterpretations of the fine details the entire image aberrations have to be taken into consideration and analytical approximations can no longer be applied to the displacement field of the defect [1].

The most important aim of the present paper, however, is to show the relation between these fine details in diffraction contrast images and the contrast features obtained from lattice fringe imaging of dislocation loops, because the fringe distortions are mainly determined by the central defect region. This allows a comprehensive systematic analysis to yield information on the local defect structure.

2. Method

The computer simulation of defocus diffraction contrast as well as of lattice fringe images of crystal defects has been carried out by the method described in the previous paper [1], combining the calculation of diffraction contrast amplitudes with the Fourier transformation formalism.

2.1. Simulation procedure

The diffraction contrast amplitudes are calculated by solving the Howie–Whelan equations using Runge–Kutta integration procedures or Thölen's matrix multiplication method. To minimize the numerical effort an amplitude interpolation procedure is applied in such a manner that only about 20% of the image pixels are integrated directly. The imaging process is described by Fourier analysis and Fourier synthesis of the amplitudes related to the image pixels, considering here the electron microscope aberrations on the basis of the contrast transfer function with special reference to the point-spread properties of the microscope.

The application of these techniques to calculate lattice fringe contrast near crystal defects is illustrated in fig. 1 [1,10]. For a Ge specimen of thickness $t = 11$ nm ($\frac{1}{4}\xi_g$, ξ_g = extinction length) bright-field (BF) and dark-field (DF) diffraction contrasts are computed for a screw dislocation having an inclination of 30° with respect to the foil surfaces ($\boldsymbol{b} = \frac{1}{2}[011]$, $\boldsymbol{b}$ = Burgers vector). The assumed incident beam direction is $\boldsymbol{e} = [\bar{1}10]$ and the diffraction vector is $\boldsymbol{g} = (111)$. For the computation of the lattice fringe contrast (LF) the interference of the bright-field and dark-field amplitudes was carried out according to the relative

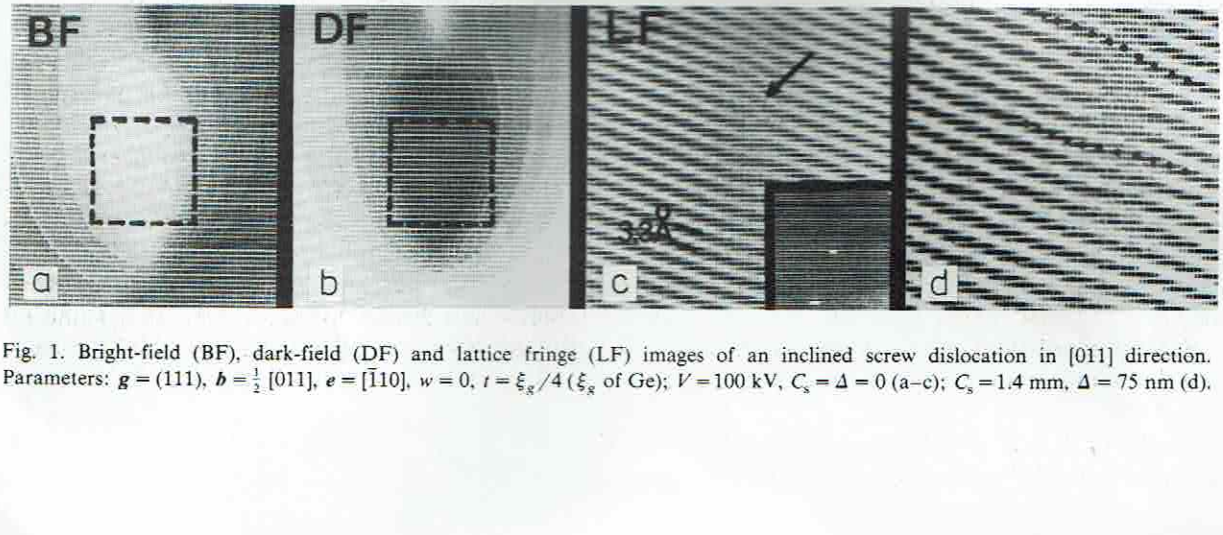

Fig. 1. Bright-field (BF), dark-field (DF) and lattice fringe (LF) images of an inclined screw dislocation in [011] direction. Parameters: $\boldsymbol{g} = (111)$, $\boldsymbol{b} = \frac{1}{2}[011]$, $\boldsymbol{e} = [\bar{1}10]$, $w = 0$, $t = \xi_g/4$ (ξ_g of Ge); $V = 100$ kV, $C_s = \Delta = 0$ (a–c); $C_s = 1.4$ mm, $\Delta = 75$ nm (d).

phase shift $\exp(2\pi i \boldsymbol{g}\cdot\boldsymbol{R})$ with the coordinate $\boldsymbol{R}$ normal to the optical axis of the microscope. The marked subunits of the BF and DF were treated by applying the interpolation procedure to the amplitudes. The inset in the LF image shows the associated calculated diffraction pattern. Confirming the $\boldsymbol{g}\cdot\boldsymbol{b}$ criterion ($\boldsymbol{g}\cdot\boldsymbol{b}=1$) an additional, terminated lattice fringe appears. If, furthermore, the experimental contrast transfer function is taken into account ($V=100$ kV, $C_s=1.4$ mm, $\Delta=75$ nm) the lattice fringe contrast is modified. In the case of this screw dislocation, for instance, it is not possible to localize the terminated fringe, because the contrast is blurred due to microscope aberrations.

The numerical calculations are supported by the analytical descriptions given in ref. [1], which allow the physical explanation of the contrast mechanism and the effects of aberrations (cf. the discussion of figs. 6 and 7). It should be mentioned here that the analytical approximations of ref. [1] can be compared with results of ref. [11], despite the different ways of approach. The damping envelope is included in the formalism of ref. [1] on the analogy of the method developed in ref. [11]. The phase terms of the dispersive expansion can be related to the terms of expansion in derivations for explaining, e.g., the significance of contrast amplification and image shift. Furthermore, in this way it is possible to distinguish the lattice fringe artifacts obtained and discussed in ref. [11] and simulated in ref. [1] for wedge-shaped crystals from the effects of aggravating truncation at the image edges.

2.2. Construction of the displacement field

For calculating the displacement field of the hexagonal dislocation loop the angular dislocation model of Yoffe is used in the form given in ref. [12]. The angular dislocation describes analytically two straight semi-infinite dislocation segments in isotropic elastic continuum enclosing an arbitrary angle and having a discontinuity of the displacements of magnitude $\boldsymbol{b}$ (Burgers vector) between them.

Six angular dislocations are combined in such a way that they form a hexagonal loop by annihilation of the dislocation segments outside the loop (cf., e.g., refs. [13,14]). This construction guarantees that the discontinuities describe a stacking fault inside the loop if $\boldsymbol{b}$ is not a perfect lattice vector. Furthermore, $\boldsymbol{b}\cdot\boldsymbol{n}$ smaller or greater than zero characterizes the vacancy or interstitial type of the loop, respectively, if $\boldsymbol{n}$ is the loop normal according to the FS/RH rule for the dislocation line directions given. The hexagonal loop is an illustrative example of defects containing more structural fine details than, e.g., the circular loop or the infinitesimal loop approximation. For the model calculations prismatic loops of Frank type are chosen, where $\boldsymbol{b}=+\frac{1}{3}[\bar{1}\bar{1}1]$ is parallel to the loop normal $\boldsymbol{n}=(\bar{1}\bar{1}1)$ describing interstitial type defects. The loop diameter is $d=2.3$ nm, i.e. approximately $0.15\xi_g$ for the extinction length (ξ_g) and absorption parameters (ξ'_g) of the Au specimen used here. The incident beam direction is $\boldsymbol{e}=[110]$ and the excited Bragg reflections are $\boldsymbol{g}=(1\bar{1}1)$ for all figures except fig. 6 where $\boldsymbol{g}=(002)$. Because of the loop inclination of about 35° with respect to the foil surfaces the depth position parameter t_0 indicates the position of the loop centre. The upper and lower parts of the loop are in depth positions which create overlapping depth effects.

3. Results

The procedure outlined above of simulating electron micrographs is applied to investigate contrast features caused by small dislocation loops characterized in section 2.2.

In figs. 2, 3 and 4 the bright-field (BF), dark-field (DF) and lattice fringe (LF) contrasts of hexagonal dislocation loops in Au are systematically studied. In order to discriminate the specimen signal itself of the final images from the aberrational influence of the electron microscope, perfect contrast transfer (in-focus $\Delta=0$, aberration-free $C_s=0$) is assumed for the three imaging modes used. For an exact Bragg orientation ($w_{1\bar{1}1}=0$) the BF, DF, and LF patterns are shown in tables, where foil thickness t and depth position t_0 of the loop are the significant specimen parameters.

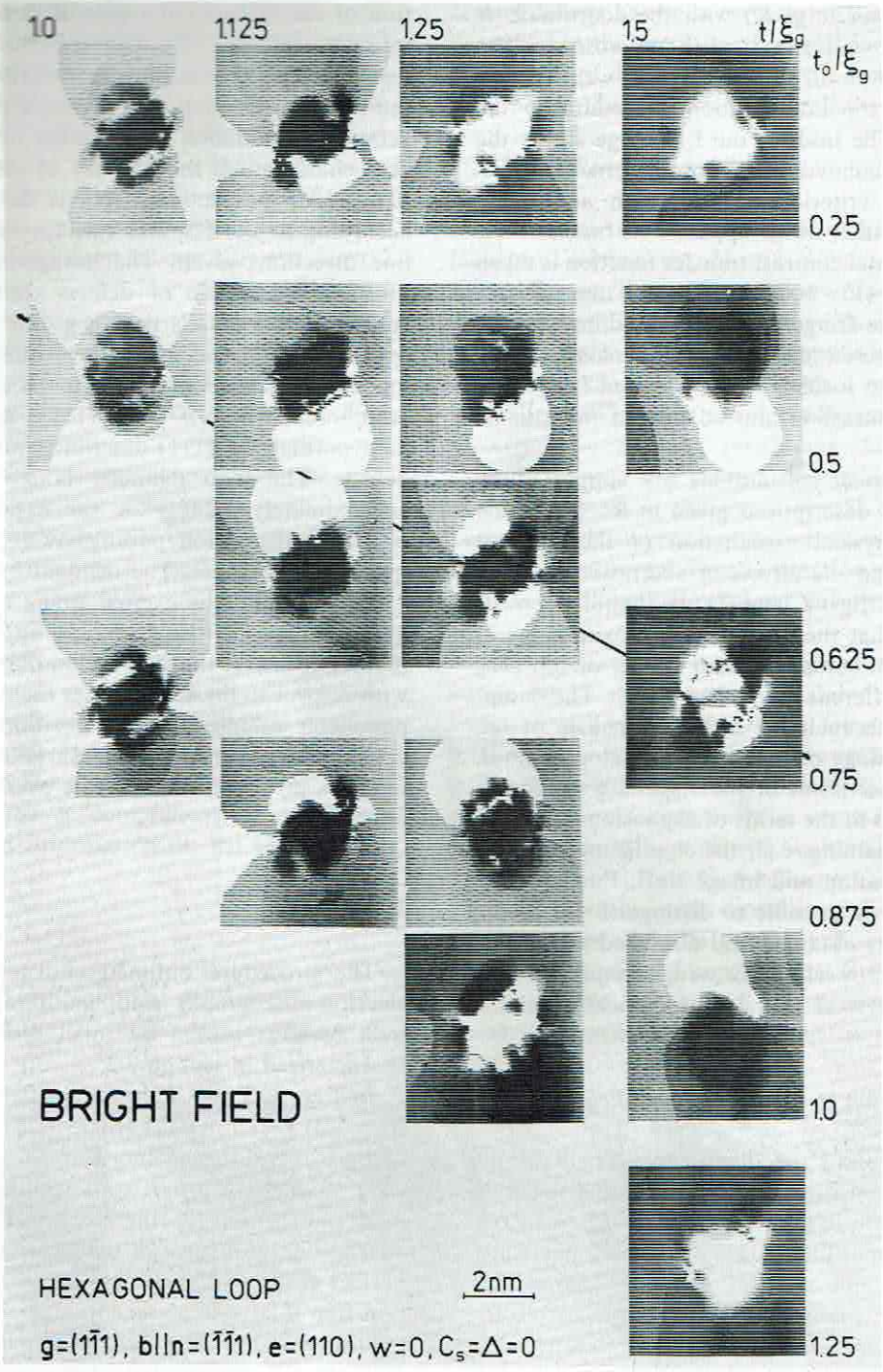

Fig. 2. Calculated bright-field images I_{000} of a hexagonal dislocation loop. Parameters: Foil thickness t/ξ_g (horizontal), depth position of defect t_0/ξ_g (vertical).

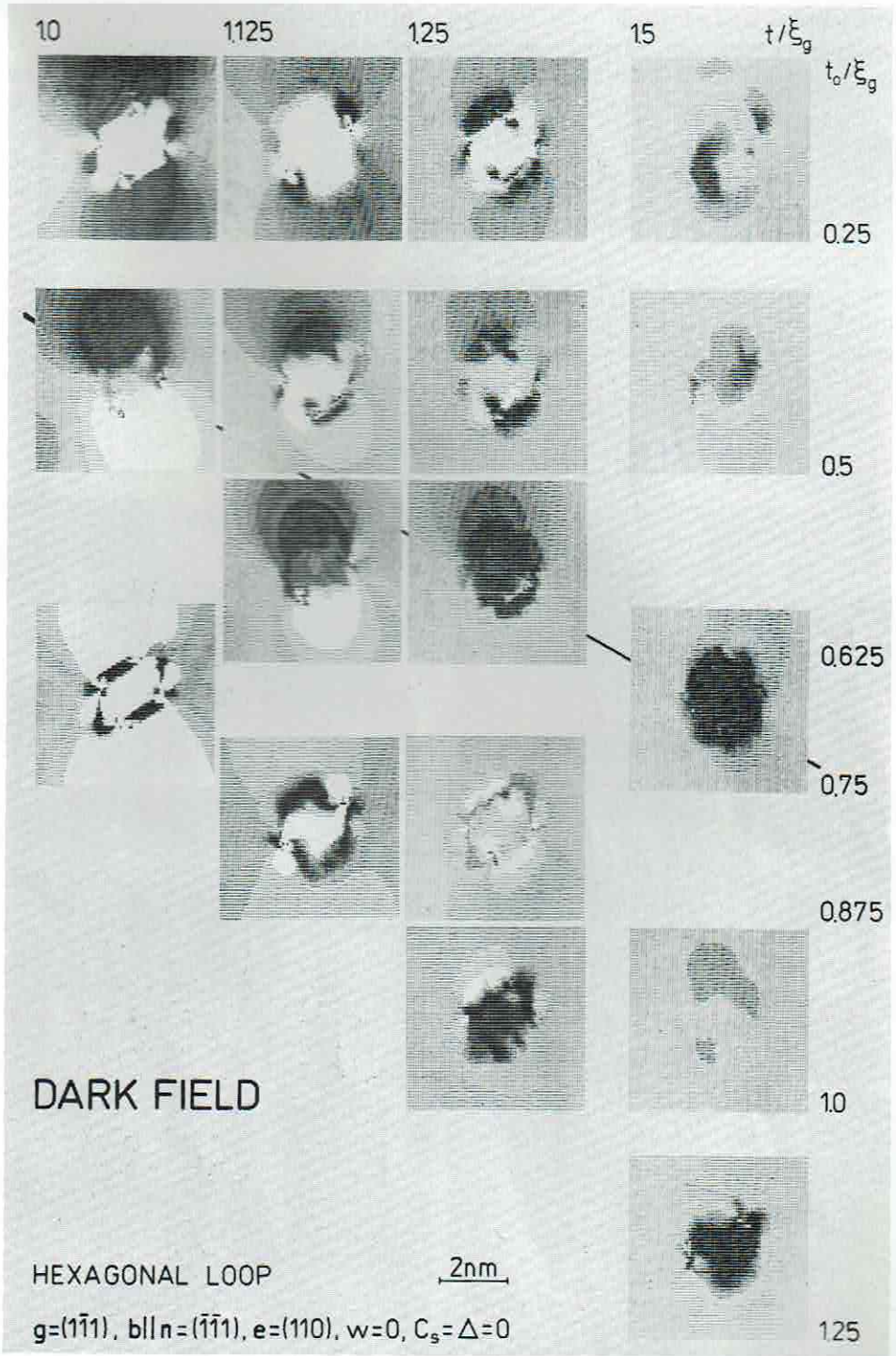

Fig. 3. Calculated dark-field images $I_{1\bar{1}1}$ of a hexagonal dislocation loop. Parameters: foil thickness t/ξ_g (horizontal), depth position of defect t_0/ξ_g (vertical).

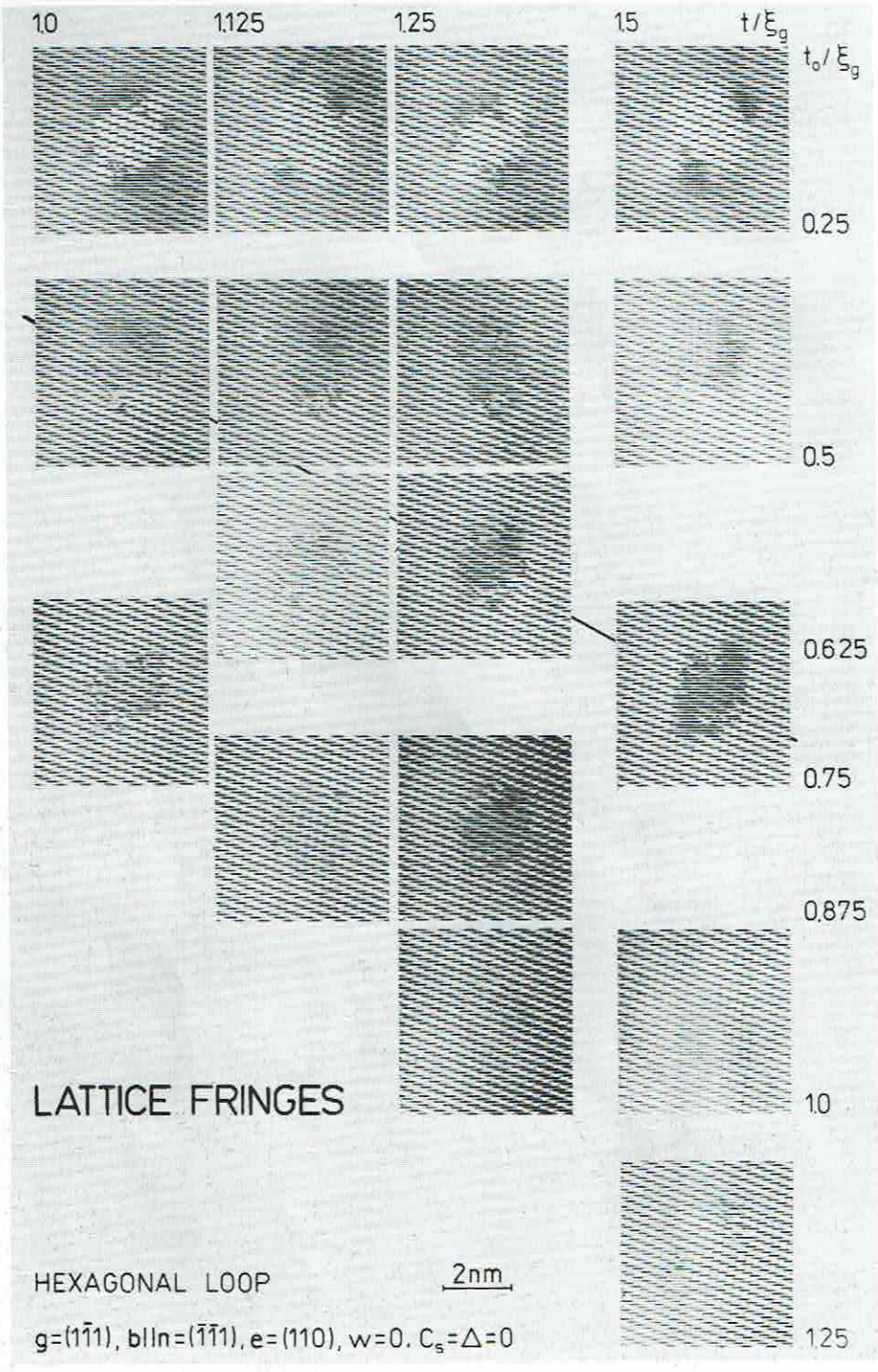

Fig. 4. Calculated (1$\bar{1}$1) lattice fringe contrast of a hexagonal dislocation loop. Parameters: foil thickness t/ξ_g (horizontal), depth position of defect t_0/ξ_g (vertical).

A selected specimen tilt series is presented in fig. 5 to investigate the effect of the deviation from the Bragg position in the image. Finally, figs. 6 and 7 reveal the influence of the contrast transfer function on the BF as well as on the LF contrast assuming factual aberrations when describing the microscope resolution limit.

3.3. Diffraction contrast

The diffraction contrast of small hexagonal loops in fig. 2 (BF) and fig. 3 (DF) may be discussed in terms of a central region and the black-white (BW) extended lobes. The BW contrasts arise due to the strains caused by the defects in the surrounding matrix under dynamical two-beam conditions [3–7]. They can be described by a black–white vector $\boldsymbol{l}$ pointing from the centre of the black lobe to that of the white one. The sign of $\boldsymbol{g} \cdot \boldsymbol{l}$, which is the product of the BW vector $\boldsymbol{l}$ and the reflection $\boldsymbol{g}$ excited, oscillates due to the depth t_0 of the defect with a $\xi_g/2$ periodicity except in a surface layer $\xi_g/4$ which is determined by relaxation effects. The angle between $\boldsymbol{g}$ and $\boldsymbol{l}$ is independent of the depth t_0 and therefore the direction of $\boldsymbol{l}$ denotes the main displacement direction which is approximately parallel to the Burgers vector projection for prismatic loops. For a fixed

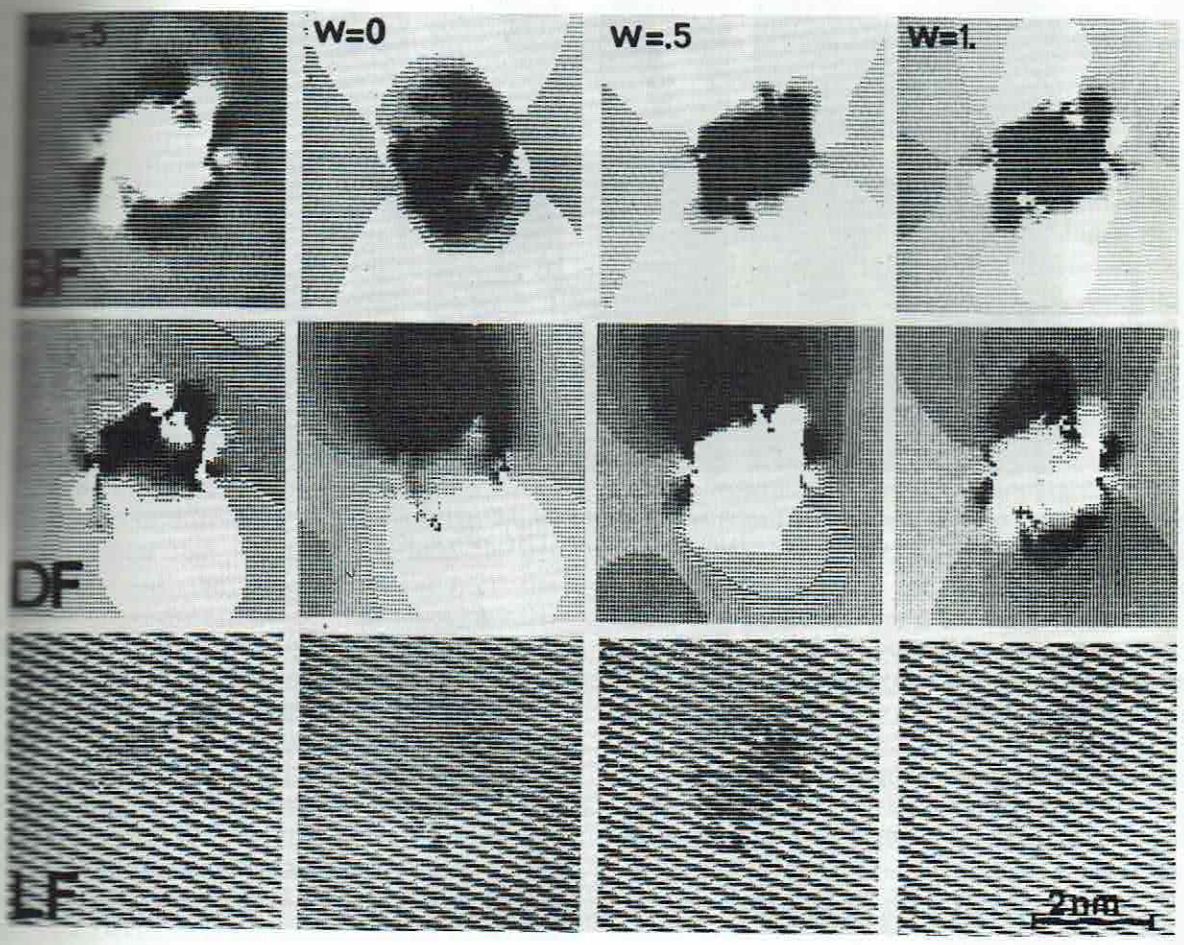

Fig. 5. Bright-field (BF), dark-field (DF) and lattice fringe (LF) images of a hexagonal dislocation loop with deviation w from the Bragg condition (tilt series). Parameters: $\boldsymbol{g} = (1\bar{1}1)$, $\boldsymbol{b} = \frac{1}{3}[\bar{1}\bar{1}1]$, $\boldsymbol{e} = [110]$, $t = 1.0\xi_g$, $t_0 = 0.5\xi_g$; $C_s = \Delta = 0$.

depth

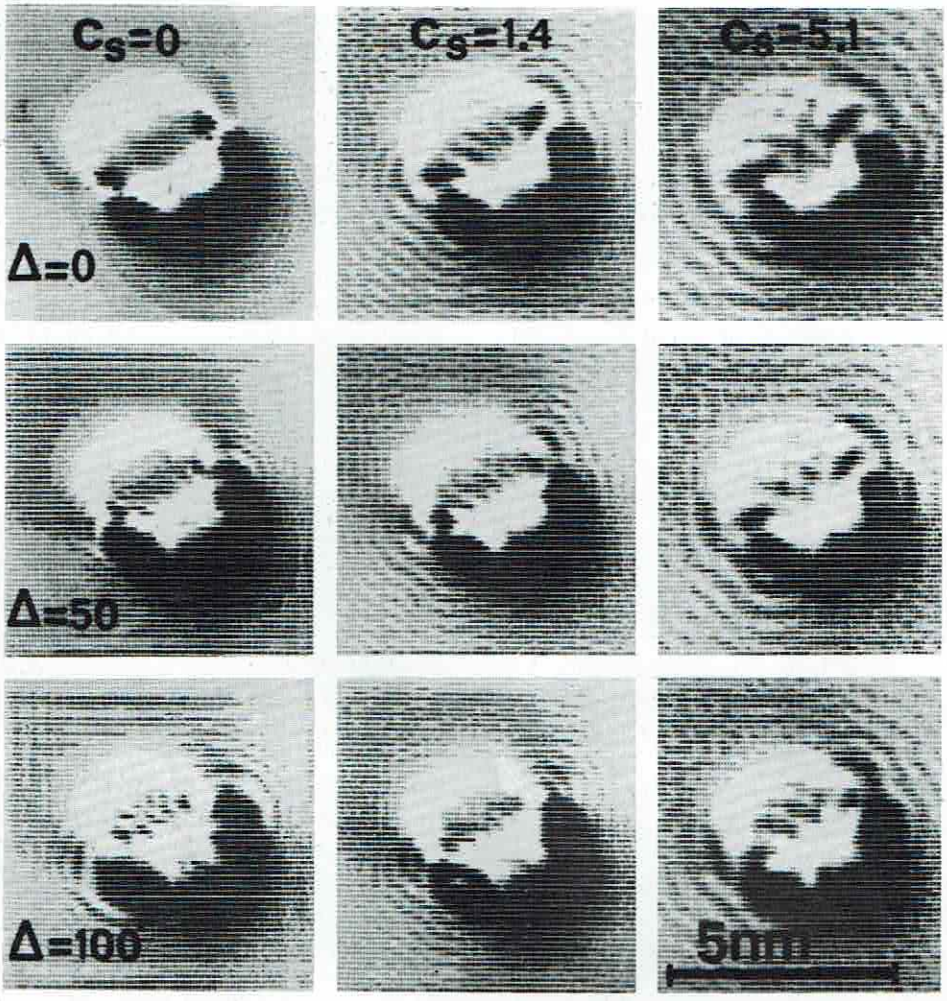

Fig. 6. Defocus (Δ) bright-field contrast of a small hexagonal loop for different C_s of the objective lens. Parameters: $\boldsymbol{g} = (002)$, $\boldsymbol{b} = \frac{1}{3}[\bar{1}\bar{1}1]$, $\boldsymbol{e} = [110]$, $t = 2\xi_g$, $t_0 = 0.125\xi_g$, $w = 0$; $V = 100$ kV.

depth t_0 the sign of the product $\boldsymbol{g} \cdot \boldsymbol{l}$ depends on the interstitial or vacancy type of the loop considered (similar to a dilation or compression centre, respectively).

Excluding the regions close to the surface ($t_0 < \xi_g/4$, $t - t_0 < \xi_g/4$) the existing depth periodicity can be characterized by the depth layers L_n of alternating BW vectors:

$$\xi_g/4 + (n-1)\xi_g/2 \leqslant t_0 \leqslant \xi_g/4 + n\xi_g/2$$

(assuming a perfect contrast transfer) [4–7]. Because of $\operatorname{sign}(\boldsymbol{g} \cdot \boldsymbol{l}) = +1$ in L_1, using our convention, the interstitial loop character is proved in the simulated BF and DF images. Analogous to the thickness fringes in wedge-shaped crystals the layer periodicity L_n is overlaid with a periodicity of the diffraction contrast depending on the specimen thickness t; the contrast for BF is maximum at $t = (2m+1)\xi_g/2$ and for DF at $t = m\xi_g$.

The intervals considered in figs. 2 and 3 of the crystal thickness $t[\xi_g, 1.5\xi_g]$ (horizontal) and of the depth of the defect $t_0[0, t]$ (vertical), are thus representative of all contrast features observable due to the periodicity of the BF and DF in

Fig. 7. Through-focus series (Δ) of lattice fringes of a hexagonal dislocation loop. Parameters: $\boldsymbol{g} = (1\bar{1}1)$, $\boldsymbol{b} = \frac{1}{3}[\bar{1}\bar{1}1]$, $\boldsymbol{e} = [110]$, $t = 1.125\xi_g$, $t_0 = 0.625\xi_g$, $w = 0$; $V = 100$ kV, $C_s = 1.4$ mm ($C_s = \Delta = 0$, for comparison).

diffraction contrast with respect to t and t_0. Accordingly, the specimen thicknesses chosen around ξ_g are appropriate for experiments as well as for the contrast calculation at higher spatial resolution applying the column approximation. The arrangements of calculated images in figs. 2 and 3 summarize the above BW contrast behaviour in BF and DF imaging. However, due to the angle of 35° between the incident beam direction $\boldsymbol{e}$ and the defect normal $\boldsymbol{n}$ of the supposed extended loop, the oscillation behaviour is overlapped here. Therefore, e.g., the expected minima of BF as well as the DF diffraction contrast at the defect depth $t_0 = \xi_g/4 + n\xi_g/2$, which are known from the infinitesimal loop approximation, are not obvious here (overlapping exceeds the minimum region of $t_0 \pm \xi_g/10$ proposed in ref. [6]).

In addition to the periodic behaviour discussed, the BF and DF diffraction contrasts in figs. 2 and 3 clearly show that for hexagonal loops in the upper half of the specimen ($t_0 < t/2$) the black–white vectors of the contrast lobes have the same sign in BF and DF patterns. If the crystal defect is below the middle of the foil the contrast vectors of BF and DF become opposite, and the image intensities are almost complementary. In the (t–t_0) table line $t_0 = t/2$ is marked; for this special depth position of the hexagonal loop the bright-field contrast patterns are symmetrical.

Compared to the background intensity, the central contrast region (inside the geometrical projection of the loop) of associated BF and DF patterns is nearly complementary. For some parameter combinations (e.g. $t = 1.0\xi_g$, $t_0 = 0.75\xi_g$) the fine structure represents the shape of the inclined hexagon, but a general classification comparable to the BW periodicities is not obvious. The phase distributions associated, however, will be revealed in the LF patterns.

3.2. Lattice fringes

While lattice fringe patterns of undistorted crystals show only black–white fringes with sinusoidal intensity profile, crystal defects cause modifications [1]. Remarkable effects in the fringe structure require significant variations of the phase difference between BF and DF amplitudes in a small area.

The resulting fine structure of the lattice fringes is detectable sufficiently rich in contrast if these phase discontinuities arise for comparable intensities in BF and DF contrasts. The contrast features in the lattice fringe images of the simulated hexagonal dislocation loops (cf. figs. 2, 3 and 4) illustrate these general considerations.

According to the crystal defect for all LF patterns, represented in fig. 4, a Burgers circuit around the complete loop does not provide any additional lattice plane in the surrounding matrix. The residual diffraction contrast of the crystal defect depends on the depth position of the loop. For the interval $t_0 < \xi_g/2$, the loop region appears bright compared to the surrounding. Approaching $t_0 = t/2$ the inner area of the defect turns dark. This effect is enhanced with increasing crystal thickness. If the loop lies below $t/2$ the residual contrast fades. This behaviour is roughly correlated

with the fact that BF and DF contrasts have the same sign (BW vector) for $t_0 \leqslant \xi_g/2$ and become opposite for $t_0 > \xi_g/2$. The direct fringe effects, which are controlled by the phase difference of BF and DF amplitudes, require comparable intensities in the corresponding image positions [1]. This condition is almost fulfilled for $t = 1.125\xi_g$ and $t = 1.25\xi_g$, on the one hand, and for $t_0 \approx t/2$, on the other hand.

There are three types of lattice contrast features:

(i) Bending of the LF at the loop, mostly accompanied by dark shadows (e.g. near the top surface $t_0 = 0.25\xi_g$).

(ii) Terminated fringes at the dislocation lines of the loops, whereby at greater distance outside the loop the terminations annihilate, confirming the Burgers circuit for closed loops (e.g. near the marked line $t_0 = t/2$).

(iii) Displacement (shift) of the fringe system inside the loop (e.g. $t = 1.0\xi_g$, $t_0 = 0.75\xi_g$; $t = 1.25\xi_g$, $t_0 = 0.875\xi_g$).

Due to the loop inclination the defect regions vary so that significant effects occur in the associated actual depth position of the loop segments. For other parameter configurations (t, t_0) more or less typical combinations of these contrast types are observable. If the defect lies near the bottom surface the lattice fringe pattern is almost undisturbed (opposite sign of BW vectors in BF and DF). A closer location of the loop to the top (e.g. $t_0 \leqslant 0.125\xi_g$) or the bottom ($t_0 \approx t$) surface of the crystal does not reveal any new systematic results, which holds also if the surface relaxation is included approximately.

3.3. Influence of specimen tilt

In the tables of figs. 2, 3 and 4 the exact Bragg orientation was assumed for all contrast investigations with varying specimen thickness and defect position. To study the influence of specimen tilt in fig. 5 the bright-field (BF), dark-field (DF) and lattice fringe (LF) contrasts of the hexagonal loop are displayed for varying excitation w of the diffraction vector $\boldsymbol{g} = (1\bar{1}1)$. This phenomenon, which has been investigated for a series of parameter combinations (t, t_0), is demonstrated for the specimen thickness $t = \xi_g$ and the depth of the loop $t_0 = 0.5\xi_g$ (see figs. 2–4). Compared to the diversity of the contrast features in figs. 2–4 a variation of the deviation parameter w around the exact Bragg orientation ($w = 0$) has a relatively small effect on the images, especially for $0 \leqslant w \leqslant 0.5$ (dynamical excitation). The characteristics of the diffraction contrast patterns, e.g. the sign of the black-white vector, remain unchanged. Furthermore, the intensity distribution inside the loop is almost unmodified for $w \geqslant 0$. However, in the BF as well as in the DF pattern shape and extension of the contrast lobes depend on the specimen tilt.

In the bottom row of fig. 5, LF images are shown, neglecting the influence of the microscope aberrations ($C_s = 0$, $\Delta = 0$). Contrary to the patterns of fig. 4, here the lattice fringe distortions with comparable structures always occur in the same loop position. The visibility of the bend as well as of terminated fringes is best for dynamical excitation, where a dark residual diffraction contrast is observable. For an increasing deviation ($|w| > 0.5$) from the Bragg orientation of the specimen the influence of the crystal defect on the LF contrast is reduced and vanishes.

3.4. Influence of microscope aberrations

In addition to the defect and specimen parameters the microscopical imaging process including the aberrations influences the final image contrast. The degree of this effect is determined by the width and spatial spectrum of the defect to be imaged and by the imaging mode (diffraction contrast, lattice fringes).

The investigation of the microscope aberrations is based on the analytical and numerical models given in ref. [1], whereby the simulation of the imaging process is applied to bright-field diffraction contrast in fig. 6 and to lattice fringes in fig. 7. As usual, the electron-optical parameters of the electron microscope are summarized in the contrast transfer function (CTF). In fig. 6 the bright-field contrast of a hexagonal loop is located at $t_0 = 15$ nm (loop centre) below the surface of a foil $t = 23$ nm thick. In detail. The exactly excited diffraction

$g = (002)$ and the incident beam direction is $e = [110]$. The loop parameters are $b = \frac{1}{3}[\bar{1}\bar{1}1]$ (Burgers vector), $n = [111]$ (loop normal), and $d = 3$ nm (loop diameter). The influence of the electron-optical contrast transfer, characterized by the most significant parameters defocus Δ and spherical aberration C_s, is simulated for an accelerating voltage of 100 kV. In the table, the lens parameter C_s is varied from left to right from $C_s = 0$ (perfect lens), over 1.4 to 5.1 mm, and the defocus from top to bottom from $\Delta = 0$ over 50 to 100 nm. This implies the ideal diffraction contrast ($C_s = 0$, $\Delta = 0$); its characteristics should be the standard for the determination of appropriate imaging conditions. An analysis of the contrast transfer function with respect to minimum additional phase shifts (Re(CTF) = 1 for a wide range of spatial frequencies) provides optimum imaging conditions for the cases $\Delta = 50$ nm, $C_s = 1.4$ mm and $\Delta = 100$ nm, $C_s = 5.1$ mm in fig. 6. Compared with the other figures, here the image modifications as well as the influence of Fresnel fringes are minimized for these parameter combinations (Δ, C_s). The effect of image aberrations on the BF diffraction contrast (cf. numerical results of fig. 6) can also be discussed by analytical approximations given in ref. [1]. Furthermore, these considerations can be extended to DF imaging and cases of tilted incident beam. The modifications of the BF intensity by the CTF can clearly be understood as a local periodic modulation of the diffraction contrast itself (amplification and shift). This is visible especially in positions having strong intensity or phase discontinuities. The distances and form of the modulation correspond to the CTF oscillations. The experimental observation of these fringe structures requires a sufficient coherence of the electron wave, i.e., a weak damping envelope of the CTF. Because of the negligible influence of the spherical angles of BF imaging the defocus term is dominant, which results in very similar effects for all parameter combinations. The column for $C_s = 0$ ($\Delta \neq 0$) in fig. 6 can be interpreted in terms of Fresnel diffraction.

For supplementing the systematic study of the bright-field, dark-field and lattice fringe contrasts of the hexagonal loop, the influence of the microscopical contrast transfer on the lattice fringe pattern is pointed out for one selected example (foil thickness $t = 1.125\xi_g$, depth position of the loop $t_0 = 0.625\xi_g$). The left part of fig. 7 (compare also fig. 5) shows the ideal two-beam interference pattern. The resulting lattice fringe amplitudes – a perfect electron microscope ($C_s = 0$, $\Delta = 0$) would assumedly register their intensity – are the input for the through-focus series ($V = 100$ kV, $C_s = 1.4$ mm, $\Delta = 0$, 51 and 86 nm, $\alpha = 0.017$ rad). The influence of the contrast transfer function emphasizes the residual diffraction contrast of the loop. Characteristic distortions of the lattice fringes remain detectable also for realistic imaging conditions. The positions of the lattice fringe effects, e.g. bendings and terminated fringes, are pointed out by dark, blurred contrast details for all defocus values. For $\Delta = 0$ and a defocus of $\Delta = 51$ nm, in particular, Fresnel fringes appear, whereas for the Scherzer focus ($\Delta = 86$ nm) the relative phase rotations are minimum over a wide band of spatial frequencies. After all, the microscopical aberrations seem to cause a slight brightening of the surrounding of the crystal defect.

4. Discussion

The associated BF, DF and LF images of figs. 2, 3 and 4, respectively, demonstrate a characteristic coincidence of the contrast features as shown above. This coincidence can be explained using eqs. (8a)–(8c) of ref. [1], which for the two-beam situation of the present calculations can be written

$$I_{LF} = I_{BF} + I_{DF} + 2(I_{BF} I_{DF})^{1/2} \times \cos(2\pi \boldsymbol{g} \cdot \boldsymbol{R} + \delta\varphi). \quad (1)$$

Here I_{BF}, I_{DF} and I_{LF} are the intensities of the BF, DF and LF images, respectively; $\boldsymbol{g}$ is the reciprocal lattice vector of the excited reflexion; and $\boldsymbol{R}$ describes the image pixel coordinates. The term $\delta\varphi$ denotes the phase difference between the transmitted (000) and diffracted ($\boldsymbol{g}$) plane waves.

As is known (see e.g. appendix of ref. [1]), I_{BF} and I_{DF} are complementary ($I_{BF} + I_{DF} = 1$), if the absorption can be neglected. A non-vanishing absorption causes a local variation of the background intensity ($I_{BF} + I_{DF}$) in the LF pattern,

which decreases with increasing depth position t_0 of the defect. The visibility of the fringes is characterized by the product $(I_{BF}I_{DF})^{1/2}$ of the BF and DF intensities, whereby the thickness oscillations of the diffraction contrast determine the general fringe structure. The depth periodicity and the fine structure of the BW contrast of both the BF and DF amplitudes describe the visibility of lattice fringes in the surrounding of the defect projection and the central region contrast.

The three types of fringe modifications discussed in section 3.2 (bending, termination, displacement) are due to the phase difference $\delta\varphi$, which therefore is the most significant term of eq. (1) in the present investigation. All examples calculated show that the outward or the inward bending of fringes as well as their termination and their shift are not unequivocally determined by the defect nature, because the phase shift strongly depends, for instance, on the depth position of the defect. In all parts of fig. 4 the location of the fringe distortions in the hexagonal loop region, however, seems to be characterized by the defect geometry. The comparison of the diffraction contrast calculations (figs. 2 and 3) with the simulated lattice fringe images (fig. 4) and with the schematic drawing of the loop projection (see fig. 8) proves this contrast behaviour. The strongest fringe distortions, which are due to the termination of fringes, are located at the inclined loop segments, whereas the strongest shifting and bending effects occur along the segments parallel to the surface. This confirms the facts that the considerable phase changes appear at the dislocation lines and that the phase ambiguity of 2π demands a dislocation segment of sufficient depth variation. If the angle between the projection of the dislocation segment and the fringe direction is large enough the phase behaviour can be correlated directly with the fringe distortions. Thus, in addition to the diffraction contrast analysis information is provided on the local defect structure.

In the broader sense, the above discussion even holds if microscope aberrations are included, as demonstrated in fig. 6 for diffraction contrast and in fig. 7 for lattice fringe imaging. For both the techniques the consideration of the imaging process modifies the contrast patterns of the simulated figs. 6 and 7 on the analogy of the [illegible] approximation in ref. [1] (e.g. blurring, [illegible] tion, shift, Fresnel fringes). The local fidel[illegible] the main features of the lattice distortion conserved even for the LF contrast, which [illegible] tive to through-focusing.

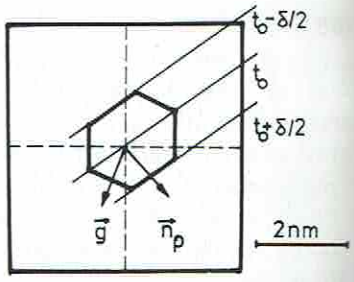

Fig. 8. Scheme of the dislocation loop projected into the [illegible] plane; $\boldsymbol{g}=(1\bar{1}1)$, $\boldsymbol{b}\|\boldsymbol{n}=(\bar{1}\bar{1}1)$, $\boldsymbol{n}_p=\boldsymbol{n}-(\boldsymbol{n}\cdot\boldsymbol{e})\cdot\boldsymbol{e}$, $\boldsymbol{e}=$ [illegible] = depth position of the loop centre, δ = depth interval [illegible] loop segments.

A more general classification of the [illegible] phenomena, however, should be possible [illegible] high-symmetry crystal defects instead of [illegible] ticular geometry assumed in the present [illegible] lations (inclined hexagonal dislocation loop[illegible] known experimental data); the reader is [illegible] to a subsequent paper on the LF simulation [illegible] small spherical precipitates.

5. Conclusions

Electron microscope contrast phenomena [illegible] focus diffraction contrast and lattice fringe [illegible] ing) of dislocation loops have been studied [illegible] application of the computer simulation [illegible] ering the specimen interaction as well as the [illegible] tron-optical imaging process. Calculated [illegible] of the bright-field, dark-field and lattice [illegible] contrasts of small hexagonal dislocation loops [illegible] compared with respect to a certain range [illegible] parameters of specimen thickness t and [illegible] position t_0 of the defect representative [illegible] entire contrast oscillation behaviour.

The fundamental features of the diffraction contrast (black-white lobes and central [illegible] inside the loop) are maintained even if the [illegible] scope aberrations are considered, but the

modified in details. Furthermore, depending on the defocus, Fresnel fringes may occur. Unlike the ideal diffraction contrast (aberration-free, in focus) the lattice fringe patterns are controlled by the local variations in the phase difference between the interfering bright-field and dark-field amplitudes. Lattice fringe distortions at the [illegible] loops (including shifting, bending and [illegible]) are shown to be associated with [illegible] diffraction contrast (e.g. black or white regions inside the loop). The fine details of the lattice fringe contrast are sensitively influenced by through-focusing. Lattice fringe distortions are blurred by the microscope aberrations because of their spatial frequency spread, but origin and local allocation are preserved.

Deviations from the exact Bragg orientation within the range of dynamical excitation ([illegible]) show that the influence of the excitation error (specimen tilt) on the final image contrast is weak. Compared to the variation of the specimen thickness and the depth position of the defect the lattice fringe distortions are confined to fixed loop regions for varying tilt.

The present work has shown that the comparison between diffraction contrast images and the lattice fringe patterns of small crystal lattice defects allows one to analyse the phase-influencing behaviour of crystal defects. Separating the different contrast features, the comprehensive study of these phase distortions supplements the defect analysis by diffraction contrast techniques.

References

[1] K. Scheerschmidt and R. Hillebrand, Phys. Status Solidi [illegible]
[2] [illegible], in: Proc. 8th European Congr. on Electron Microscopy, Budapest, 1984, Vol. I, Eds. A. Csanady, P. [illegible] p. 175.
[3] [illegible] and L.M. Brown, Phil. Mag. 8 (1963) 1083, [illegible]
[4] [illegible], [illegible] Wilkens and M. Rühle, Phys. Status Solidi [illegible]
[5] [illegible] and L.M. Brown, J. Phys. Radium 27 C3 [illegible]
[6] M. Wilkens, Identification of Small Defect Clusters, in: Diffraction and Imaging Techniques in Material Science, Eds. S. Amelinckx, R. Gevers and J. Van Landuyt (North-Holland, Amsterdam, 1978) p. 223.
[7] [illegible], W.D. Cooper and J.J. Hren, Oak Ridge National Laboratory ORNL/TM-7619 Report 1981.
[8] [illegible], Phys. Status Solidi (a) 66 (1980) 479.
[9] W. [illegible] and M. Wilkens, Phys. Status Solidi (a) 89 [illegible]
[10] K. Scheerschmidt and R. Hillebrand, in: Proc. 11th Hungarian Conf. on Diffraction, Győr, 1982, p. 126.
[11] L.D. Marks, Ultramicroscopy 12 (1984) 237.
[12] K. Scheerschmidt and J. Heydenreich, Phys. Status Solidi [illegible]
[13] K. Scheerschmidt, in: Proc. 11th Intern. Congr. on Crystallography, Warsaw, 1978, p. 262.
[14] D.K. Saldin and M.J. Whelan, Phil. Trans. Roy. Soc. London A292 (1979) 53.